

UC San Diego

UC San Diego Previously Published Works

Title

Strong Metasurface-Josephson Plasma Resonance Coupling in Superconducting $\text{La}_{2-x}\text{Sr}_x\text{CuO}_4$

Permalink

<https://escholarship.org/uc/item/1bc8682z>

Journal

Advanced Optical Materials, 7(21)

ISSN

2195-1071

Authors

Schalch, Jacob S
Post, Kirk
Duan, Guangwu
et al.

Publication Date

2019-11-01

DOI

10.1002/adom.201900712

Peer reviewed

Strong Metasurface–Josephson Plasma Resonance Coupling in Superconducting $\text{La}_{2-x}\text{Sr}_x\text{CuO}_4$

Jacob S. Schalch, Kirk Post, Guangwu Duan, Xiaoguang Zhao, Young Duck Kim, James Hone, Michael M. Fogler, Xin Zhang, Dmitri N. Basov, and Richard D. Averitt*

Terahertz spectroscopy of the c -axis Josephson plasma resonance (JPR) in high-temperature cuprates is a powerful probe of superconductivity, providing a route to couple to and interact with the condensate. Electromagnetic coupling between metasurface arrays of split ring resonators (SRRs) and the JPR of a $\text{La}_{2-x}\text{Sr}_x\text{CuO}_4$ single crystal ($T_c = 32$ K) is investigated. The metasurface resonance frequency (ω_{MM}), determined by the SRR geometry, is swept through the JPR frequency ($\omega_{\text{JPR}} = 1.53$ THz) using a series of interchangeable tapes applied to the same single crystal. Terahertz reflectivity measurements on the resulting hybrid superconducting metamaterials (HSMs) reveal anticrossing behavior characteristic of strong coupling. The experimental results, validated with numerical simulations, indicate a normalized Rabi frequency of $\Omega_R = 0.29$. Further, it is shown that HSMs with $\omega_{\text{MM}} > \omega_{\text{JPR}}$ provide a route to couple to hyperbolic waveguide modes in c -axis cuprate samples. This work informs future possibilities for optimizing the coupling strength of HSMs and investigating nonlinear superconductivity under high field terahertz excitation.

1. Introduction

In recent decades, considerable effort has gone into the study of strong coupling of light and matter.^[1–4] Initially, strong

light–matter coupling was primarily confined to the realm of atomic and molecular physics. However, advances in fabricating micron scale plasmonic structures, microcavities, and probing the resultant properties have opened up new possibilities for dressing quantum materials in order to achieve strong coupling effects.^[5–7] Metasurfaces, typically consisting of arrays metallic split ring resonators (SRRs), have received attention for manipulation of electromagnetic (EM) waves in the far field^[8,9] and can be fabricated by standard lithographic techniques on any surface of sufficient quality. Importantly, the strong resonant enhancement and localization of EM waves in the near field of SRRs provide a route for coupling to nearby materials.^[10] This strategy has been employed to demonstrate coupling to cyclotron resonances,^[11]

phonons,^[12] and electronic transitions in semiconductors.^[13] A telltale sign of strong coupling between the metamaterial (MM) resonator and the quantum state is the appearance of polariton modes split by the Rabi vacuum frequency Ω_R .^[14] The splitting provides a direct measure of the coupling strength, and corresponds to the frequency at which virtual photons are exchanged between the constituents comprising the coupled system.^[15,16] Recent work in which metamaterials couple to the cyclotron resonance (ω_C) of semiconductor 2DEGs achieved a normalized coupling of $\Omega_R = 0.87$,^[17] and even reached beyond unity coupling of $\Omega_R = 1.43$.^[18] In this latter regime known as ultrastrong coupling, new possibilities for the manipulation of dressed quantum states are possible, including the observation of correlated virtual photon pairs,^[19] nonclassical radiation from thermal sources,^[20] and sideband cooling of quantum order parameters^[21] among others. Superconductors have emerged as another type of system fruitful for the study of light–matter coupling^[22] offering a pathway to interrogate or manipulate superconductivity.^[23]

High-temperature superconductivity and its interactions with below-gap EM fields have been extensively investigated. Specifically, layered high- T_c superconducting cuprates such as $\text{La}_{2-x}\text{Sr}_x\text{CuO}_4$ (LSCO) have demonstrated complex phenomena associated with interlayer Josephson effects.^[24,25] Below T_c , LSCO can be modeled as a stack of superconducting CuO_2 layers weakly coupled along the c -axis.^[26] The system behaves as a series of Josephson junctions, exhibiting a collective phase


Dr. J. S. Schalch, Dr. K. Post, Prof. M. M. Fogler, Prof. R. D. Averitt
Department of Physics
University of California San Diego
La Jolla, CA 92093, USA
E-mail: raveritt@physics.ucsd.edu

Dr. G. Duan, Dr. X. Zhao, Prof. X. Zhang
Department of Mechanical Engineering
Boston University
Boston, MA 02215, USA

Prof. Y. D. Kim
Department of Physics
Kyung Hee University
Seoul 02447, Republic of Korea

Prof. J. Hone
Department of Mechanical Engineering
Columbia University
New York, NY 10027, USA

Prof. D. N. Basov
Department of Physics
Columbia University
New York, NY 10027, USA

 The ORCID identification number(s) for the author(s) of this article can be found under <https://doi.org/10.1002/adom.201900712>.

DOI: 10.1002/adom.201900712

oscillation at the Josephson plasma resonance (JPR) frequency. The JPR typically lies in the THz regime, and can be identified by a characteristic plasma edge in reflection measurements, corresponding (as shown next) to a zero in the dielectric response.^[27] The JPR in LSCO has been studied extensively, and manipulation of the superconducting phase via optical excitation of the JPR has been accomplished by microwave cavity cooling,^[28] optical pumping,^[29] and high field THz excitation.^[30] However, dressing of the JPR with microstructures has remained elusive.^[31] Epitaxial thin films of LSCO which would be suitable for the deposition of metamaterials have an exposed *ab*-plane, precluding the possibility of coupling incident light to the *c*-axis JPR.^[32] Fortunately, large single crystals of LSCO can be grown and cut to expose a large *c*-axis surface. However, direct fabrication of metasurfaces on such precious samples using photolithography would make it challenging to perform systematic studies of light–matter coupling.

We present evidence of strong coupling between the *c*-axis JPR of LSCO and the inductive-capacitive (LC) resonance of a SRR metasurface through observation of an avoided resonance crossing. At 15% Sr doping, and well below $T_c = 32$ K (10 K) the JPR resonance frequency is $\omega_{\text{JPR}} = 1.53$ THz. In order to parametrically sweep the LC resonance frequency across the JPR, we fabricated a series of flexible and interchangeable metasurface tapes (MSTs) (see the Experimental Section). The MSTs were adhered to a LSCO single crystal with the *c*-axis in plane (Figure 1). We fabricated three MSTs: One with a resonant frequency greater than ω_{JPR} , one near ω_{JPR} , and one below ω_{JPR} . We performed Fourier transform infrared (FTIR) spectroscopy measurements in reflection on the resulting HSMMs and validated the results with numerical simulations, indicating a normalized Rabi frequency of $\Omega_R = 0.29$. Furthermore, as described next, we used these simulations to extend these results for arbitrary metamaterial resonance frequency to unambiguously delineate the avoided resonance crossing, explore the near-field

behavior of the HSMMs, and investigate routes toward excitation of hyperbolic waveguide modes in LSCO.

2. Results

The metamaterial tapes consist of a flexible polyimide tape patterned with 200 nm thick Au SRRs, where the linewidth, periodicity, gap size, and edge length of the SRR are scaled uniformly to achieve the three desired frequencies. The fabrication begins with polyimide spin-coated (thickness of 8 μm) onto a silicon wafer coated with a sputtered silicon nitride film to facilitate the removal of the polyimide from the substrate.^[33] Subsequently, the periodic array of SRRs consisting of 200 nm thick gold is patterned using direct laser writing followed by gold deposition and lift-off process. The nominal dimensions of the three metamaterial tapes are shown in Table 1. The MM tapes can be peeled off of the substrate (Figure 1a), and pressed onto the LSCO such that the capacitive gap is parallel to the *c*-axis. Figure 1c shows a schematic of the HSMM. In this geometry, the polyimide serves as a dielectric spacer layer between the SRR and LSCO, preventing the LSCO from shorting the plasmonic resonance of the SRR. The LSCO single crystal was grown by the travelling-solvent floating-zone method.^[34] The large single crystal is oriented by LAUE diffraction and with the *a*–*c* plane as the surface. We perform reflection spectroscopy measurements of the LSCO and HSMM samples with the polarization parallel to the *c*-axis using a Bruker FTIR IFS-66 spectrometer.

The LSCO JPR response was first characterized in the absence of the MSTs. At $T = 10$ K (well below $T_c = 32$ K), the characteristic reflectivity feature associated with the JPR occurs at $\omega_{\text{JPR}} = 1.53$ THz as shown by the black dots in Figure 2a. The *c*-axis response of layered cuprates is often expressed using the two-fluid model of the permittivity

$$\epsilon_c(\omega) = \epsilon_\infty - \frac{\omega_s^2}{\omega^2} - \frac{\omega_n^2}{\omega^2 + i\gamma_{\text{st}}\omega} \quad (1)$$

where $\epsilon_\infty = 27$ corresponds to the *c*-axis high-frequency dielectric constant, $\omega_s = 8$ THz is the plasma frequency of the superconducting carriers, $\omega_n = 21.3$ THz, and $\gamma_{\text{st}} = 150$ THz are, respectively, the plasma frequency and the scattering rate of normal state carriers. The numerical values are suitable at $T = 10$ K.^[24] Thus, the expression includes a term for the lossless tunneling supercurrent and normal carriers with scattering. Furthermore, it is well known that in near optimally doped cuprates, spatial inhomogeneities result in a distribution of JPR frequencies. This in turn results in a broadened loss

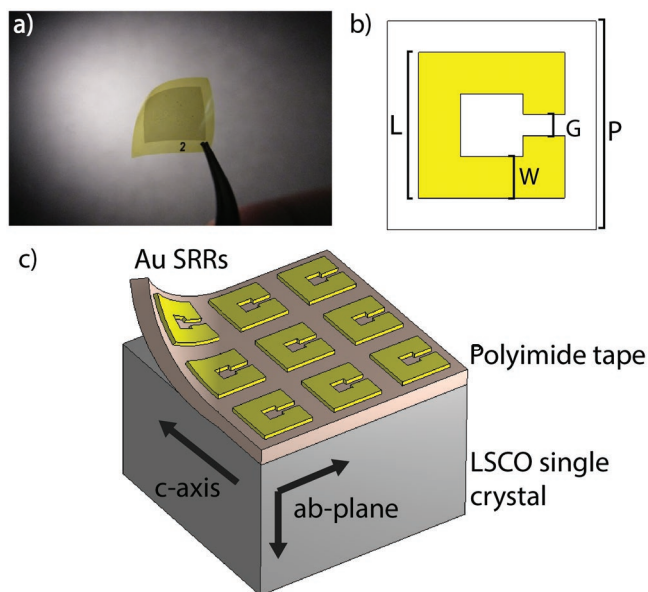


Figure 1. a) A photo of the MST with SRRs. b) Schematic of metamaterial unit cell. c) Schematic of hybrid superconducting metamaterial.

Table 1. Dimensions of the MSTs. The resonant frequencies at 300 K after adhering to the LSCO crystal. For all three samples, the nominal thickness of the polyimide is 8 μm .

	<i>P</i> [μm]	<i>L</i> [μm]	<i>W</i> [μm]	<i>G</i> [μm]	ω_{LC} [THz]
Tape 1	20	14	3.8	2.0	2.90
Tape 2	36	25.2	8.5	3.6	1.90
Tape 3	52	8.5	11.5	5.2	1.24

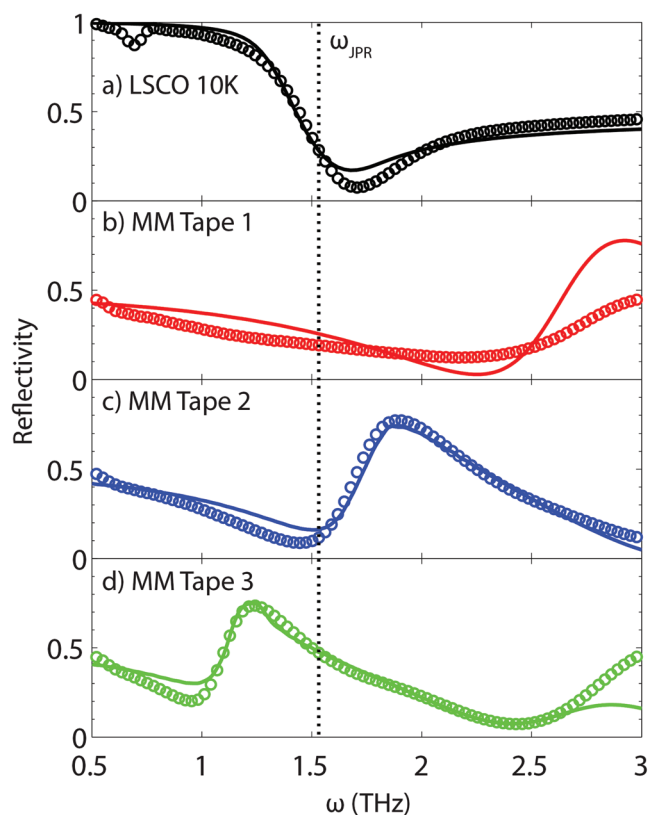


Figure 2. a) Reflectivity of LSCO at 10 K (circles) with a two-fluid model fit (solid line), and b–d) MSTs 1, 2, and 3 on LSCO at 300 K (red, blue, and green circles) and FDTD simulations (solid lines).

function and associated JPR plasma edge. We broaden the JPR with a Gaussian distribution with a width of 0.5 THz in order to more closely model the experimentally observed response.^[35] The solid black line in Figure 2a shows the fit to the reflectivity computed from this model. Some discrepancies between the model and the measurements persist due to simplifications made in this model and imperfect referencing.

Subsequently, the MSTs were adhered to the LSCO crystal and room-temperature FTIR measurements were performed to identify the resonant frequencies of the MM tapes in the absence of the JPR (Figure 2b–d). The LC resonance is the lowest frequency resonance of the metamaterial, corresponding to the reflection maxima which occur at $\omega_{\text{MM1}} = 3$ THz, $\omega_{\text{MM2}} = 1.9$ THz, and $\omega_{\text{MM3}} = 1.2$ THz for MST 1, 2, and 3, respectively. Likewise, this is the frequency for which the enhancement of the incident EM fields in the capacitive gap of the SRR will be largest. We model these results using the commercial finite difference time domain (FDTD) solver CST^[36] and find good agreement (solid lines). In these simulations, gold is modeled as a lossy metal with conductivity $\sigma = 4.56 \times 10^7 \text{ S m}^{-1}$, polyimide as a lossy dielectric with permittivity $\epsilon_{\text{PI}} = 3.5 + i0.01$, and the LSCO above T_c is modeled as an isotropic dielectric with permittivity of $\epsilon_\infty = 27$. Overall, the agreement between experiment and simulation is reasonable and demonstrates that, above T_c , the electromagnetic response is what is expected for SRRs placed on top of a nominally dielectric substrate (i.e., the c -axis is effectively dielectric

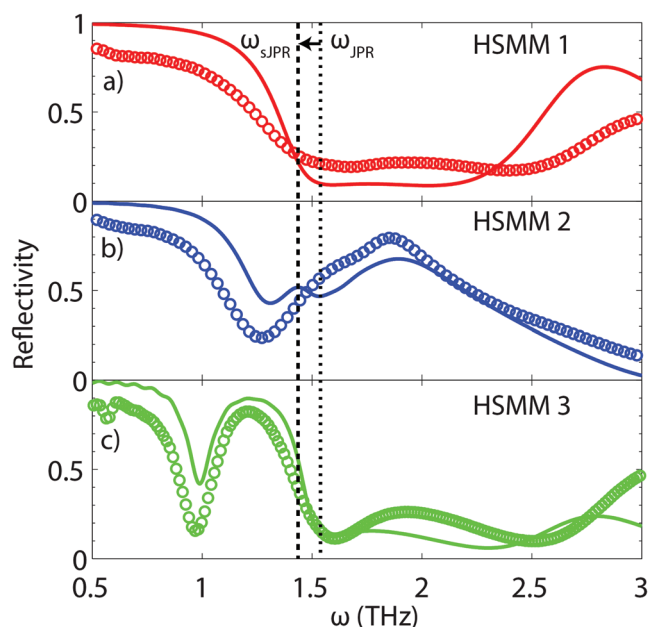


Figure 3. a–c) Reflectivity of MSTs on LSCO at 10 K for MM tape 1, 2, and 3 (circles), and corresponding FDTD simulations (solid lines). A dotted vertical line indicates the screened JPR at $\omega_{\text{sJPR}} = 1.44$ THz.

and dominates the overall electromagnetic response, while the ab -plane conductivity has little effect).

The reflectivity of each of the HSMs was measured at 10 K ($< T_c$) as shown in Figure 3a–c. In the presence of the MSTs, the JPR is redshifted because of the polyimide layer to $\omega_{\text{sJPR}} = \omega_{\text{JPR}} \sqrt{\epsilon_\infty / (\epsilon_\infty + \epsilon_{\text{PI}})} = 1.44$ THz (Figure 3 vertical line). HSM 1 (red circles) has two significant spectroscopic features: The peak in reflectivity at $\omega_{\text{MM1}} \approx 3$ THz is virtually identical to the one that appears in spectra above T_c (Figure 2b). Likewise, the Drude-like reflectivity edge at ω_{sJPR} differs only marginally from the bare LSCO (Figure 2a). In Figure 3b, the results for HSM 2 (blue circles) are shown. There is a reflection maxima characteristic of a MM resonance at ≈ 1.9 THz (similar to the room temperature case in Figure 2c) and, additionally, a plasma-like edge at ≈ 1.3 THz which is clearly redshifted relative to $\omega_{\text{sJPR}} = 1.44$ THz. For HSM 3 (green circles, Figure 3c), JPR plasma edge is again similar to bare LSCO, but there is a pronounced and narrow reflection minimum at ≈ 1 THz. Interpreting these features and identifying spectroscopic evidence of strong coupling is nontrivial and will be clarified in the following sections.

We compare these results to full wave FDTD simulations (solid lines). In these simulations, the gold and polyimide are modeled as in the previous section, whereas the LSCO at 10 K is modeled as an anisotropic superconductor. This c -axis response is as described before (Equation (1)) while the ab -plane permittivity used in the simulation is determined from experimental measurements.^[37] For the c -axis complex permittivity, we use the parameters determined from the fit to Figure 2a with Equation (1) including the Gaussian broadening previously mentioned. We find fair agreement between the experimental reflectivity and simulations with much of the discrepancy likely due to the disagreement between the modeled and measured

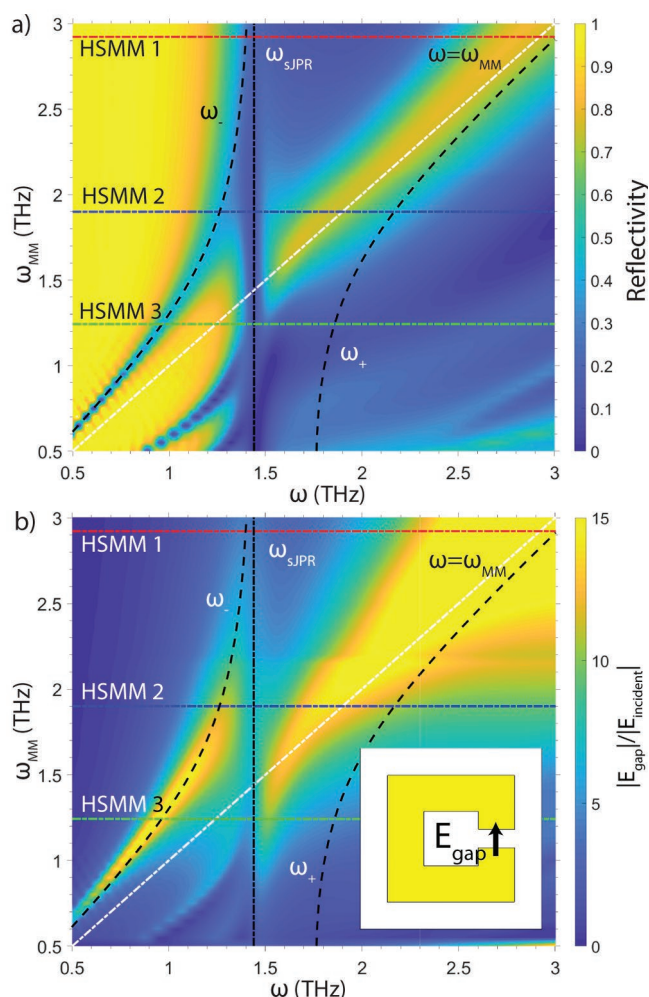


Figure 4. Extended FDTD simulation results showing a) reflectivity, and b) electric field enhancement in the metamaterial capacitive gap, as a function of arbitrary metamaterial tape resonant frequency. MST frequencies used in experimental measurements are marked by dotted horizontal lines in red, blue, and green for tape 1, 2, and 3, respectively. A vertical black dotted line marks ω_{sJPR} , and a diagonal line tracks $\omega = \omega_{MM}$. Black dashed lines track the coupled polaritons of the dielectric function from Equation (3) at ω_+ and ω_- . While the simulated spectrum and field enhancements track the lower polariton branch well, features connected to the upper polariton do not agree with the analytical result. Inset: The location on the SRR where the fields are probed.

c-axis properties (see Figure 2a). Nonetheless, the agreement is sufficiently good that we can investigate the electrodynamic response in greater detail using simulations with finer tuning of the SRR geometry (and therefore the resonance frequency) than is practical in experiment.

We performed additional simulations as shown in Figure 4 to retrieve reflectivity spectra for MSTs of arbitrary resonant frequency to gain additional insight into the experimental results. Here, ω_{MM} denotes the frequency of the MST resonance on LSCO above T_c where $\epsilon_\infty = 27$. The diagonal dashed white line tracks $\omega_{MM} = \omega$. The horizontal lines at ω_{MM1} (red), ω_{MM2} (blue), and ω_{MM3} (green) correspond to the three resonance frequencies for which experimental measurements were performed (i.e., Figure 3a–c). The vertical dotted line denotes

$\omega_{sJPR} = 1.44$ THz. At frequencies above the JPR, the *c*-axis of the LSCO is insulating, and the metamaterial LC resonance manifests as a broad reflection maximum, as is typical for a MM on a dielectric substrate. But as ω_{MM} approaches at ω_{sJPR} , this reflection feature is suppressed. For $\omega < \omega_{sJPR}$, a narrow absorption band emerges, indicative of the LC resonance of a metamaterial in the presence of a conducting ground plane. Below the JPR, the *c*-axis LSCO surface is highly conductive exhibiting near unity reflection. As a result, this narrow absorption band can be intuitively understood using the same formalism as for metamaterial perfect absorbers.^[38] This reflection minima emerges from the plasma edge at $\omega_{sJPR} = 1.44$ THz, and diverges from it, eventually asymptotically approaching ω_{MM} at low frequencies. For lower values of ω_{MM} , additional resonant absorption modes emerge below ω_{sJPR} first at $\omega = 1.3$ THz and $\omega_{MM} = 0.9$ THz and again at $\omega = 1.3$ THz and $\omega_{MM} = 0.5$ THz. These are associated with the higher order dipole and quadrupole modes of the MM, respectively. Clearly, a rich electromagnetic response is observed upon sweeping ω_{MM} from 0.5 to 3.0 THz.

3. Discussion

Additional insight can be obtained by considering a simplistic, yet analytical, effective medium dielectric response for the HSMM. The optical response of the HSMM is assumed to be the sum of two oscillators: a Drude response representing the Josephson plasmon and a Lorentzian oscillator corresponding to the MST. The total effective permittivity parallel to the *c*-axis can be expressed as

$$\epsilon_{tot} = \epsilon_{eff} - \frac{\omega_s^2}{\omega^2 + i\gamma_a\omega} + \frac{F(\omega_{MM})}{\omega_{MM}^2 - \omega^2 - i\gamma_b\omega} \quad (2)$$

where $\epsilon_{eff} = \epsilon_\infty + \epsilon_{PI} = 30.5$ is the effective permittivity at high frequency. The second term is the Drude response of the Josephson plasmon, with $\omega_s = 8$ THz and $\gamma_a = 0.28$ THz. In lieu of an additional Drude term for normal carriers (as in Equation (1)), the contribution of the normal carriers in the LSCO at low frequencies is adequately captured by adding an effective damping term to the Josephson plasmon. While the Josephson plasmon is still nominally lossless, this damping term broadens the plasma edge as when the normal carrier term is present. The third term is a Lorentzian to model the metamaterial, where ω_{MM} is the MM LC resonance frequency and the damping is given by $\gamma_b = 0.8$ THz. $F(\omega_{MM})$ acts as a fitting parameter but generally represents the MM oscillator strength which is related to the geometry and the filling fraction of resonators.^[10,39] This simplified model is adequate for the present purposes to gain some insight into the effective response of the HSMMs as a function of tuning the resonance frequency of the Lorentzian term.

The Lorentzian MM response has a pole at $\omega = \omega_{MM}$, corresponding to a transverse mode associated with the resonance of the metamaterial. The JPR response (i.e., the first two terms of Equation (2)) has no finite frequency transverse modes, but exhibits a longitudinal mode when the sum of the terms equals zero, which occurs at the screened JPR $\omega_{sJPR} = 1.44$ THz. Coupling between the JPR and the MST response leads to

mode splitting and the emergence of a new longitudinal (polaritonic) mode. This is analogous to the situation that occurs upon doping a semiconductor such that the plasma frequency approaches an optical phonon mode.^[40,41]

To obtain the longitudinal mode coupling, we simply set $\epsilon_{\text{tot}} = 0$, and solve to obtain the roots

$$\omega_{\pm} = \frac{1}{\sqrt{2}} \left[\omega_{\text{MM}}^2 + \frac{(\omega_s^2 + F)}{\epsilon_{\text{eff}}} \pm \sqrt{\left(\omega_{\text{MM}}^2 + \frac{(\omega_s^2 + F)}{\epsilon_{\text{eff}}} \right)^2 - \frac{4\omega_s^2 \omega_{\text{MM}}^2}{\epsilon_{\text{eff}}}} \right]^{\frac{1}{2}} \quad (3)$$

The two polariton solutions ω_- and ω_+ are shown as curved black lines in Figure 4. We use F as a parameter to fit the lower polariton ω_- . For large values of ω_{MM} , the lower polariton follows the longitudinal mode of the LSCO at ω_{SJPR} . But as ω_{MM} decreases and approaches $\omega_{\text{MM}} = \omega_{\text{SJPR}}$, the polariton undergoes an avoided crossing, before asymptotically approaching the MM transverse mode along $\omega = \omega_{\text{MM}}$. While the lower polariton solution closely tracks the reflection minima, the reflectivity features associated with upper polariton show little correspondence to ω_+ . This asymmetry and suppression of coupled polaritons is not unusual in coupled systems where radiative losses depend strongly on frequency.^[42] Both F and γ , strongly depend on both ω and ω_{MM} resulting in considerable discrepancies between the simulations and our model. In particular, above ω_{SJPR} (where the c -axis of the LSCO acts as a dielectric), the resonance has a low quality factor as is typical for SRRs above a dielectric material, resulting in deviations between the simulations and the simple predictions of Equation (3). Conversely, below ω_{SJPR} , the c -axis is metallic and the quality factor of the resonance is significantly higher (as is typical for SRRs above a metallic surface, i.e., metamaterial perfect absorbers) and thus the polariton is clear.

By evaluating the polariton frequencies at $\omega_{\text{MM}} = \omega_{\text{SJPR}}$, we can also estimate the strength of the normalized coupling constant as

$$\frac{(\omega_+ - \omega_-)}{2\omega_{\text{SJPR}}} = \Omega_R = 0.29 \quad (4)$$

This splitting and coupling can be viewed classically as a simple consequence of the linear absorption and dispersion of the effective dielectric function, or as a manifestation of vacuum Rabi splitting.^[43–45] Making a clear-cut distinction between weak and strong coupling in this scenario is difficult, particularly due to the frequency-dependent damping of the MM. Nevertheless, a normalized coupling constant of $\Omega_R = 0.29$ falls within the strong coupling regime as defined by Novotny^[46] even for conservative choices of oscillator parameters.

This simple effective medium analysis is a broad approximation, but nonetheless provides some insight into the nature of the avoided crossing and the role various parameters play in determining the coupling. The terms under the square root (Equation (3)) determine the magnitude of the splitting between the coupled modes, and thus the coupling strength. In particular, the oscillator strength of the MM tape, F , is dependent on the design parameters of the MM and can, therefore, be optimized to achieve stronger coupling. We note that this effective medium

model is intended to provide a simple and intuitive analytical approach to understanding the response observed in experiment and in the full wave electromagnetic simulations. This approach does not, however, account for higher frequency modes of the SRRs, which are apparent at small values of ω_{MM} . Nor does it capture the strong asymmetry of the polaritons mentioned previously. However, it is intriguing that for the experimental data for HSMM 3, there is a pronounced peak at 1.9 THz (Figure 3c). This peak does not appear in the full wave simulations (Figure 4a), but does agree with the black dashed line corresponding to the upper polariton. Nonetheless, further experimental work will be required to more fully elucidate the full details of the coupling. Indeed, a more complete analytical analysis should be possible, but is beyond the scope of the present work.^[47,48]

To gain further insight into JPR/SRR coupling, it is useful to examine the near field. We performed FDTD simulations to probe the fields in the SRR gaps as a function of metamaterial tape frequency ω_{MM} . We present the result in Figure 4b. Because this field enhancement is at a maximum when the SRR is resonantly excited, it can serve as a useful proxy to identify the coupled polaritons of the HSMM. Whereas in the reflection spectra, polariton modes may appear either as reflection maxima or minima, the local field enhancement magnitude is a positive quantity associated with absorption. This approach unambiguously shows a broad peak which begins at high frequencies and approaches ω_{SJPR} as ω_{MM} is decreased. But at the crossing the peak is strongly suppressed. Meanwhile, below the JPR, field enhancement peak emerges close to ω_{SJPR} but avoids the crossing point before asymptotically approaching ω_{MM} at low frequencies. With this approach, an asymmetric avoided crossing is obvious and validates our previous interpretation of the evolution of the HSMM reflection spectra.

We can further support this interpretation by examining the surface currents and electric field distributions elsewhere in the HSMM at specific frequencies (Figure 5). In Figure 5a, we examine the field enhancement spectrum for each of the HSMMs for which experiments were performed (see horizontal lines in Figure 4b). The peaks in the local field enhancement occur at nearly the same frequencies where features in the far-field spectroscopy appear. For each of the HSMMs, open (closed) circles in Figure 5a indicate frequencies at which minima (maxima) in the experimental reflectivity spectra occur that, as previously discussed, are tied to the lower (upper) polaritons. The close correspondence between the field enhancement maxima and the spectral features observed experimentally lends additional evidence to our interpretations of the experimental spectra.

Figure 5b,c shows the electric field distributions in the LSCO and the surface currents on the SRRs for HSMM 2, where the MM resonance is tuned close to the JPR and, as described before, $\Omega_R = 0.29$. Figure 5b shows the fields and currents for HSMM 2 sampled at the lower polariton frequency (1.3 THz), corresponding to the open blue circle in Figure 5a. The current (black arrows) circulates around the SRR, characteristic of the LC resonance. At this frequency (1.3 THz < ω_{SJPR}), the c -axis is metallic while the ab -plane is superconducting meaning that only evanescent waves are supported. The electric field parallel to the c -axis (color) decreases exponentially into the LSCO, and is confined to the first few micrometers of the crystal.

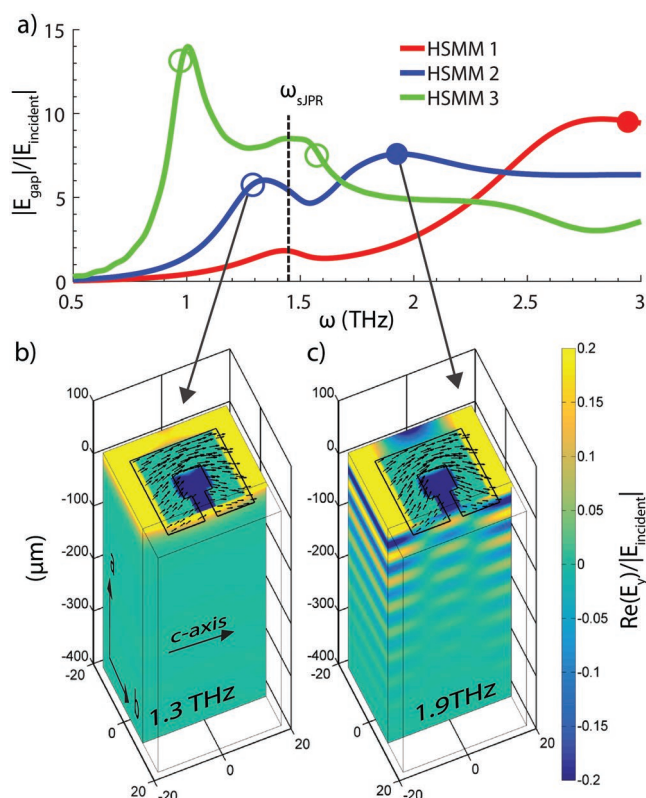


Figure 5. a) The field enhancements relative to the incident field at the SRR gap for each of the tested HSM 1 (red), HSM 2 (blue), and HSM 3 (green). Open circles correspond to frequencies of local minima in experimental results while closed circles indicate local maxima. b,c) (Top) Surface current densities (black arrows) and electric fields parallel to the *c*-axis (color) for HSM 3 sampled at 1.3 and 1.9 THz, corresponding to the circled features in the spectrum.

Figure 5c shows the fields and currents for HSM 2 sampled at the upper polariton frequency (1.9 THz), corresponding to the closed blue circle in Figure 5a. Though well separated from the lower polariton, the currents on the SRR are circulating as before. This indicates that though this frequency corresponds to an entirely different spectroscopic feature, the LC nature of the SRR resonance is nevertheless retained. However, inside the LSCO at this frequency (1.9 THz), the electrodynamics are entirely different. Namely, a propagating mode is observed with pronounced subwavelength structure, persisting over a considerable propagation distance. Two planar nodes in the electric field appear parallel to the *ab*-plane. Though this behavior is only incidentally connected to the coupling, these noteworthy electrodynamics warrant further investigation.

Above ω_{SJPR} the *c*-axis permittivity is positive, while the *ab*-plane permittivity remains large and negative (i.e., superconducting). Thus, above the JPR resonance, LSCO constitutes a hyperbolic medium for which $\epsilon_{\text{ab}}\epsilon_{\text{c}} < 0$. In a hyperbolic medium, EM waves from finite sources (i.e., a dipole) propagate in an unusual fashion which depends on both the relative signs of the permittivity on the axis of anisotropy (the *c*-axis in this case) and other axes, as well as the polarization of the source relative to the axis of anisotropy.^[49,50] These are known as hyperbolic waveguide modes (HWM). When the axis

of anisotropy has positive permittivity and a dipole is oriented parallel to it, the hyperbolic media support radiating waves similar to that of a point dipole in an ordinary dielectric, but with conical regions above and below the dipole in which fields are entirely excluded. Relative to the axis of anisotropy, the angle of this excluded region is given by $\tan^2\theta < -\epsilon_{\text{ab}}/\epsilon_{\text{c}}$. In the case of LSCO at 10 K and at 1.9 THz, $\theta \approx \pi/2$, so fields propagate almost exclusively along the *ab*-plane with minimal angular dispersion.

Returning to the metasurface, we consider a cross section parallel to the *c*-axis and through the capacitive gap of the SRR. The segment spanning the capacitive gap of the SRR constitutes an extended dipole oriented parallel to the axis of anisotropy (*c*-axis). Similarly, the segments between the edge of the SRR and the unit cell boundary (i.e., between SRRs in adjacent unit cells) act as a similar dipole, but with a phase shift of π . In Figure 5c, we can understand the checkerboard pattern of fields which propagate into the LSCO as being a highly directional projection of the fields produced on the plane of the SRRs. After dispersing slightly in the polyimide, the field distribution which reaches the LSCO surface is “locked-in,” and propagates a significant distance parallel to the *ab*-plane, while retaining its subwavelength structure. It should be noted that this phenomenon does not appear in a metasurface over an ordinary dielectric substrate nor in an isotropic medium with a Drude-like response. We note that though the fields in the vicinity of the SRR have fine structure as previously described, the wave decays to a uniform plane wave over a very short propagation distance, in contrast to what is shown in Figure 5c. These interesting near-field phenomena could inform methods whereby HWMs are launched from a metasurface excited by a far-field pulse. Such modes propagate over a distance exceeding 100 μm , so conceivably they could be measured on the opposite side of a thin crystal. It should also be noted that rich dispersive properties emerge in the case of arrays of dipoles in the vicinity of a hyperbolic media, but this is beyond the scope of the current work.^[51]

4. Conclusions

Our initial measurements on HSMs demonstrate the viability of achieving strong light–matter coupling between the Josephson plasmon in LSCO with interchangeable MSTs. We have demonstrated spectroscopic evidence of strong coupling with a normalized coupling of $\Omega_{\text{R}} = 0.29$ and performed simulations both to extend the spectroscopic results as well as examine the near-field electromagnetic field distributions and interactions between the LSCO and MSTs. Additionally, in the near-field simulations, we have observed evidence of hyperbolic waveguide modes emerging in the LSCO.

In general, this work demonstrates the utility of using removable MSTs for achieving interactions between the MMs and solid state systems. This may prove particularly useful in situations where the availability, surface quality, or sensitivity of a crystal makes direct deposition of MMs onto its surface (i.e., through lithography) untenable. Our results offer guidance for the design of future iterations of HSMs that aim to achieve higher coupling constants through tailoring of the spatial and

temporal characteristics of the hybrid mode, that is, through thinner dielectric membranes or higher Q metasurfaces. It will also be important to perform more thorough experimental characterization of the HSMM electrodynamic response to more fully understand the nature of the coupling beyond the simulations and simplistic analytical model presented here.

Finally, due to the intrinsic nonlinearities associated with Josephson plasma oscillations, we can apply this approach in conjunction with high field THz excitation in order to explore the complex nonlinear interactions in HSMMs that are likely to emerge.^[29,52] Likewise, this could provide an exciting avenue for the direct experimental observation of hyperbolic waveguide modes using near-field techniques, for instance, with THz near-field microscopy.^[31,53]

Acknowledgements

The authors acknowledge support from the Department of Energy Basic Energy Sciences (DOE-BES) (DE-SC0018218) for work performed at UC San Diego and Columbia University. The authors thank Boston University Photonics Center for technical support and the National Science Foundation (ECCS-1810252) for work performed at Boston University.

Conflict of Interest

The authors declare no conflict of interest.

Keywords

Josephson plasmonics, metamaterials, superconductivity, THz, ultrastrong coupling

Received: April 27, 2019

Revised: July 29, 2019

Published online:

- [1] P. Forn-Díaz, L. Lucas, E. R. Ortega, J. Kono, E. Solano, **2018**, arXiv:1804.09275.
- [2] A. F. Kockum, A. Miranowicz, S. De Liberato, S. Savasta, F. Nori, **2018**, arXiv:1807.11636.
- [3] X. Li, M. Bamba, Q. Zhang, S. Fallahi, G. C. Gardner, W. Gao, M. Lou, K. Yoshioka, M. J. Manfra, J. Kono, *Nat. Photonics* **2018**, *12*, 324.
- [4] G. Günter, A. A. Anappara, J. Hees, A. Sell, G. Biasiol, L. Sorba, S. De Liberato, C. Ciuti, A. Tredicucci, A. Leitenstorfer, R. Huber, *Nature* **2009**, *458*, 178.
- [5] C. Ciuti, G. Bastard, I. Carusotto, *Phys. Rev. B* **2005**, *72*, 115303.
- [6] S. De Liberato, C. Ciuti, I. Carusotto, *Phys. Rev. Lett.* **2007**, *98*, 103602.
- [7] M. V. Muravev, I. V. Andreev, I. V. Kukushkin, S. Schmult, W. Dietsche, *Phys. Rev. B* **2011**, *83*, 075309.
- [8] D. Schurig, J. J. Mock, B. J. Justice, S. A. Cummer, J. B. Pendry, A. F. Starr, D. R. Smith, *Science* **2006**, *314*, 977.
- [9] J. B. Pendry, D. Schurig, D. R. Smith, *Science* **2006**, *312*, 1780.
- [10] G. R. Keiser, H. R. Seren, A. C. Strikwerda, X. Zhang, R. D. Averitt, *Appl. Phys. Lett.* **2014**, *105*, 081112.
- [11] G. Scalari, C. Maissen, D. Turčinková, D. Hagenmüller, S. De Liberato, C. Ciuti, C. Reichl, D. Schuh, W. Wegscheider, M. Beck, J. Faist, *Science* **2012**, *335*, 1323.
- [12] D. J. Shelton, I. Brener, J. C. Ginn, M. B. Sinclair, D. W. Peters, K. R. Coffey, G. D. Boreman, *Nano Lett.* **2011**, *11*, 2104.
- [13] Y. Todorov, A. M. Andrews, R. Colombelli, S. De Liberato, C. Ciuti, P. Klang, G. Strasser, C. Sirtori, *Phys. Rev. Lett.* **2010**, *105*, 196402.
- [14] I. Carusotto, C. Ciuti, *Rev. Mod. Phys.* **2013**, *85*, 299.
- [15] C. Weisbuch, M. Nishioka, A. Ishikawa, Y. Arakawa, *Phys. Rev. Lett.* **1992**, *69*, 3314.
- [16] C. Ciuti, G. Bastard, *Phys. Rev. B* **2005**, *72*, 115303.
- [17] C. Maissen, G. Scalari, F. Valmorra, M. Beck, J. Faist, S. Cibella, R. Leoni, C. Reichl, C. Charpentier, W. Wegscheider, *Phys. Rev. B* **2014**, *90*, 205309.
- [18] A. Bayer, M. Pozimski, S. Schambeck, D. Schuh, R. Huber, D. Bougeard, C. Lange, *Nano Lett.* **2017**, *17*, 6340.
- [19] C. M. Wilson, G. Johansson, A. Pourkabirian, J. R. Johansson, T. Duty, F. Nori, P. Delsing, *Nature* **2011**, *479*, 376.
- [20] A. Ridolfo, S. Savasta, J. M. Hartmann, *Phys. Rev. Lett.* **2013**, *110*, 163601.
- [21] M. Aspelmeyer, T. J. Kippenberg, F. Marquardt, *Rev. Mod. Phys.* **2014**, *86*, 1391.
- [22] X. Gu, A. F. Kockum, A. Miranowicz, Y. Liu, F. Nori, **2017**, arXiv:1707.02046.
- [23] L. S. Bilbro, R. Valdés Aguilar, G. Logvenov, O. Pelleg, I. Božović, N. P. Armitage, *Nat. Phys.* **2011**, *7*, 298.
- [24] S. Uchida, K. Tamasaku, *Phys. Rev. E* **1996**, *53*, R21.
- [25] A. M. Gerrits, A. Wittlin, V. H. M. Duijn, A. A. Menovsky, J. J. M. Franse, P. J. M. van Bentum, *Physica C* **1994**, *1117*, 235.
- [26] D. N. Basov, T. Timusk, *Rev. Mod. Phys.* **2005**, *77*, 721.
- [27] As mentioned in the text, the JPR is not a resonance in terms of being a pole in the dielectric response. Indeed, it corresponds to a zero of the dielectric response. The unfortunate nomenclature arises from the fact that the Josephson response can be modeled as a resonant LRC circuit, with the capacitance C arising from the insulating spacer between the copper oxygen planes, the inductance L arising from the condensate response, and the resistance R from the uncondensed quasiparticles.
- [28] J. Hammer, M. Aprili, I. Petković, *Phys. Rev. Lett.* **2011**, *107*, 017001.
- [29] D. Nicoletti, E. Casandruc, Y. Laplace, V. Khanna, C. R. Hunt, S. Kaiser, S. S. Dhesi, G. D. Gu, J. P. Hill, A. Cavalleri, *Phys. Rev. B* **2014**, *90*, 100503(R).
- [30] S. Rajasekaran, E. Casandruc, Y. Laplace, D. Nicolletti, G. D. Gu, S. R. Clark, D. Jaksch, A. Cavalleri, *Nat. Phys.* **2016**, *12*, 1012.
- [31] Y. Laplace, S. Fernandez-Pena, S. Gariglio, J. M. Triscone, A. Cavalleri, *Phys. Rev. B* **2016**, *93*, 075152.
- [32] H. T. Stinson, J. S. Wu, B. Y. Jiang, Z. Fei, A. S. Rodin, B. S. Chapler, A. S. Mcleod, A. H. Castro-Neto, Y. S. Lee, M. M. Fogler, D. N. Basov, *Phys. Rev. B* **2014**, *90*, 014502.
- [33] H. Tao, C. M. Bingham, A. C. Strikwerda, D. Pilon, D. Shrekenhamer, N. I. Landy, K. Fan, X. Zhang, W. J. Padilla, R. D. Averitt, *Phys. Rev. B* **2008**, *78*, 241103(R).
- [34] K. Oka, M. J. V. Menken, Z. Tarnawski, A. A. Menovsky, A. M. Moe, T. S. Han, H. Unoki, T. Ito, Y. Ohashi, *J. Cryst. Growth* **1994**, *137*, 479.
- [35] S. V. Dordevic, S. Komiya, Y. Ando, D. N. Basov, *Phys. Rev. Lett.* **2003**, *91*, 167401.
- [36] Computer Simulation Technology, Microwave Studio Suite, <https://www.cst.com/products/cstmws> (accessed: November 2016).
- [37] S. Tajima, Y. Fudamoto, T. Kakeshita, B. Gorshunov, V. Železný, K. M. Kojima, M. Dressel, S. Uchida, *Phys. Rev. B* **2005**, *71*, 094508.
- [38] H. Chen, *Opt. Express* **2012**, *20*, 7165.

- [39] C. E. Kriegler, M. S. Rill, S. Linden, M. Wegener, *IEEE J. Sel. Top. Quantum Electron.* **2010**, 16, 367.
- [40] B. B. Varga, *Phys. Rev.* **1965**, 137, A1896.
- [41] K. S. Singwi, M. P. Tosi, *Phys. Rev.* **1966**, 147, 658.
- [42] V. M. Muravev, I. V. Andreev, I. V. Kukushkin, S. Schmult, W. Dietsche, *Phys. Rev. B* **2011**, 83, 075309.
- [43] Y. Zhu, D. J. Gauthier, S. E. Morin, Q. Wu, H. J. Carmichael, T. W. Mossberg, *Phys. Rev. Lett.* **1990**, 64, 2499.
- [44] S. R. K. Rodriguez, *Eur. J. Phys.* **2016**, 37, 025802.
- [45] L. Novotny, *Am. J. Phys.* **2010**, 78, 1199.
- [46] R. Houdré, *Phys. Status Solidi B* **2005**, 242, 2167.
- [47] B. Y. Jiang, L. M. Zhang, A. H. Castro Neto, D. N. Basov, M. M. Fogler, *J. Appl. Phys.* **2016**, 119, 054305.
- [48] A. E. Koshelev, L. N. Bulaevskii, M. P. Maley, *Phys. Rev. B* **2000**, 62, 14403.
- [49] A. Poddubny, I. Iorsh, P. Belov, Y. Kivshar, *Nat. Photonics* **2013**, 7, 948.
- [50] A. S. Potemkin, A. N. Poddubny, P. A. Belov, Y. S. Kivshar, *Phys. Rev. A* **2012**, 86, 023848.
- [51] C. Guclu, S. Campione, F. Capolino, *Phys. Rev. B* **2014**, 89, 155128.
- [52] S. Rajasekaran, J. Okamoto, L. Mathey, M. Fechner, V. Thampy, G. D. Gu, A. Cavalleri, *Science* **2018**, 359, 575.
- [53] A. P. Schnyder, S. Ryu, *Phys. Rev. B* **2011**, 84, 060504.